Stanford Exploration Project, Report 77, November 17, 1997, pages 1–248

Kirchhoff prestack impedance inversion: a gas reservoir pilot study

David E. Lumley[1]

keywords: *impedance, velocity, inversion, reflectivity, gas, prestack, elastic, approximation, amplitudes, modeling, least squares*

ABSTRACT

Estimation of subsurface material properties and their spatial variation is important in hydrocarbon exploration and detection, and crucial to subsequent reservoir characterization and management. I conduct a pilot study to test my prestack impedance inversion theory and algorithms on a marine data set from the Gulf of Mexico, acquired over a known producing gas reservoir. First, I perform a high-resolution migration velocity analysis at every adjacent CMP location, and estimate a migration/inversion velocity model which is optimal in a Monte Carlo automatic velocity fitting technique. Next, I perform a least-squares Kirchhoff migration to estimate the angle-dependent reflectivity at each subsurface point, followed by a linearized Zoeppritz elastic parameter inversion for relative contrasts in compressional and shear wave impedance. Finally, I combine the P and S impedance contrast maps into a single image indicative of anomalous gas saturation levels. This hydrocarbon indicator correlates very well with the known gas reservoir interval, and suggests lateral heterogeneity of gas saturation along the reservoir unit.

INTRODUCTION

Hydrocarbon reservoirs are increasingly recognized as spatially heterogeneous entities, in terms of pore-fluid content, pore-fluid saturation, porosity, permeability, lithology, and structural control. Knowledge of these reservoir parameters and their spatial variation is critical in the evaluation of the total volume of hydrocarbon reserves in place, in understanding and predicting physical processes in the reservoir such as fluid flow and heat transfer, and in projecting and monitoring reservoir fluid production and recovery as a function of time.

Conventional approaches to estimating reservoir properties are mainly obtained

[1]**email:** not available

through borehole measurements such as: rock cores, rock cuttings, geophysical well logs, and reservoir engineering pressure tests. These data are valuable in that they represent *in situ* measurements, but unfortunately only sample a very small fraction of the total reservoir volume (e.g., Nur, 1989).

Surface seismic data, on the other hand, potentially sample the entire reservoir volume, although at a lower resolution and in a *remote*, as opposed to in situ, manner. Traditionally, surface seismic data are used as an imaging tool to make seismic-derived geologic maps of the reservoir target zone. These images are subsequently interpreted by reservoir geologists in terms of structure, stratigraphy, and major fault patterns, in order to provide some structural control to the reservoir model. However, relatively little work has been done to directly relate seismic reflection data to the reservoir mechanical property contrasts which generate the seismic reflections.

Previous work

Tarantola (1986) proposed a nonlinear strategy to perform full waveform inversion of seismic reflection data directly for elastic parameters, essentially bypassing the reflectivity estimation step. This approach was implemented by Crase et al. (1990) on a 2-D marine data set, and was *extremely* computer intensive. Furthermore, because this one-step approach offers no intermediate processed steps to check for quality control, their results may be somewhat ambiguous in terms of the reliability of the elastic impedance results, robustness of multiple suppression, and sensitivity to the initial background velocity model.

Beydoun and Mendes (1989) greatly reduced the magnitude of complexity of the full nonlinear inverse problem by assuming a linear relation between elastic parameter perturbations and seismic reflection data under the Born approximation. Although their method is much more tractable than that of Tarantola et al., it is not clear that the Born approximation is valid for seismic reflection data, in which impedance contrasts may be large and nonlinear point scatterer-to-scatterer interaction (i.e., reflection) may be significant.

However, since elastic reflectivity, and not elastic parameters themselves, is linearly related to seismic reflection data amplitudes, it may be natural to pose the inverse problem as first inverting for elastic angle-dependent reflection coefficients, and then subsequently performing a much-simplified nonlinear inversion of Zoeppritz-like reflectivity, in order to estimate elastic parameters (e.g., Lumley and Beydoun, 1991).

Cunha (1992) developed an elastic reverse-time migration method based on finite differences to forward model and continue elastic displacement wavefields. Estimates of elastic angle-dependent reflectivity were attempted by performing numerical correlations of attributes of the continued wavefields. Although theoretically appealing, Cunha's preliminary results were inconclusive. Possible disadvantages to Cunha's method include its prohibitive computational expense, and significant potential for instability in the presence of noise due to its fundamental shot-domain implementation.

In a recent work, de Bruin (1992) uses an w-x finite difference depth migration method to make migrated midpoint gathers as a function of depth and ray parameter. His migrated gathers show excellent recovery of angle-dependent reflectivity amplitudes in synthetic tests. Unfortunately, de Bruin's method interprets the ray parameter values in terms of reflection angles, which is appropriate only in a 1-D medium. In a 2-D (or 3-D) medium, de Bruin must raytrace the reflection angles external to the migration/inversion procedure, using a posteriori information about the depth model structure and dip.

In previous works, I formulate the inverse problem in the space-time constant offset domain, which offers the potential for enhanced numerical inversion stability (Lumley and Beydoun, 1991; Lumley, 1992a; and Lumley 1993). The least-squares integral solutions are compressed by the use of ray-valid WKBJ Green's tensors (Aki and Richards, 1980), thus reducing the number of floating point operations ultimately required to perform wavefield continuation and correlation. Both the angle-dependent reflectivity, *and* the associated reflection angles, are estimated directly from the data. This approach is related to the Kirchhoff integral formulation of Parsons (1986), which is based on the work of Beylkin (1985) and Bleistein (1987), except that I consider elastodynamic vector wave propagation as opposed to acoustics, and find a potentially robust least-squares solution as opposed to a potentially unstable "direct" integral inverse. The theoretical results of Lumley and Beydoun (1991) and Lumley (1993) form the basic foundation for the algorithms and results presented in this real data study.

Outline

This paper proceeds as follows. First, I review the essential theory underlying the angle-dependent reflectivity estimation, and the subsequent impedance inversion. Next, I show an application of the theory and algorithms to a marine data set acquired in the Gulf of Mexico over a known producing gas reservoir. This real data pilot study includes a high-resolution migration velocity analysis, a prestack angle-dependent reflectivity estimation, and a subsequent linearized Zoeppritz inversion for relative contrasts in P and S impedance. Finally, I calculate a single hydrocarbon indicator map which correlates well with the known gas interval, and suggests lateral variations in gas saturation. The results of this study seem to validate the theory and algorithms I use here.

THEORY

Forward problem

The theory underlying this study is more fully discussed in Lumley and Beydoun (1991) and Lumley (1993). I assume a forward model for a "generalized" PP reflectivity, R_{PP}, which combines elements of plane wave reflection and Rayleigh-Sommerfeld diffraction theory. I define a differential volume element of R_{PP} as

$$R_{PP} = \frac{iw}{\alpha} \grave{P}\acute{P} \cos\phi_s \cos\phi_r \ , \tag{1}$$

for $|\phi_s, \phi_r| \leq \pi/2$, and zero otherwise. Here, w is angular frequency, α is compressional velocity, $\grave{P}\acute{P}$ is the Zoeppritz PP plane wave reflection coefficient and ϕ_s (ϕ_r) is the angle between the incident source (receiver) ray and the specular ray in Figure **??**. Θ is the specular angle of reflection. Equation (1) can be integrated over the subsurface volume to model the reflected scalar wavefield:

$$U(\mathbf{x}_r; \mathbf{x}_s, w) = \int_V A_s A_r R_{PP} e^{iw\tau} dV \ , \tag{2}$$

where $\mathbf{x}_s$ ($\mathbf{x}_r$) is the shot (receiver) coordinate, and τ is the total traveltime from source to reflection point to receiver. A_s (A_r) is the WKBJ amplitude factor along the source (receiver) leg of the raypath to the subsurface reflection point $\mathbf{x}$, and incorporates the amplitude effects of source (receiver) directivity, geometric spreading, transmission loss, and intrinsic high-frequency Q attenuation. All of these quantities are obtained by raytracing through the background migration velocity model.

Inverse problem

The least-squares inverse problem is formulated as follows. A constant-offset l_2 misfit energy functional can be defined as

$$E = \int_w \int_{\mathbf{x}_m} \left[D(\mathbf{x}_m; \mathbf{x}_h, w) - U(\mathbf{x}_m; \mathbf{x}_h, w) \right]^2 \, d\mathbf{x}_m \, dw \ , \tag{3}$$

where $D(\mathbf{x}_m; \mathbf{x}_h, w)$ is a recorded constant offset section. Minimizing (3) with respect to $\grave{P}\acute{P}$ and Θ leads to two coupled normal equations. The equations can be decoupled by the stationary phase (high-frequency) approximation, in which the major contribution to (2) occurs near the specular point when $\phi_s \approx \phi_r \approx 0$. In this case, the $\grave{P}\acute{P}$ equation can be solved independently of Θ, and the result can be backsubstituted into the original normal equation for Θ.

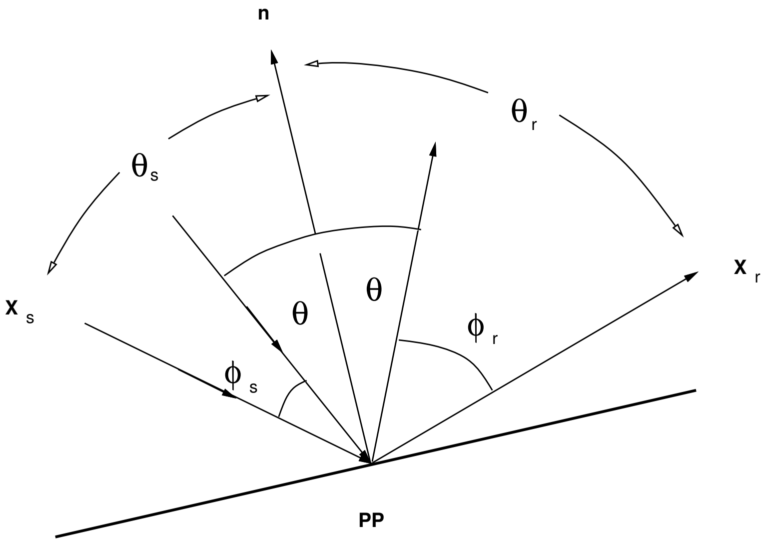

Figure 1: Ray geometry for generalized reflection and diffraction. david3-geom [NR]

Reflectivity estimation

Under the stationary phase approximation, the $\grave{P}\acute{P}$ equation is in the standard linear form: $\mathbf{d} = \mathbf{F}\mathbf{m}$. This has a well-known damped least-squares Gauss-Newton solution: $\mathbf{m} \approx -\mathbf{H}^{-1}\mathbf{g} = (\mathbf{F}'\mathbf{F} + \epsilon^2)^{-1}\mathbf{F}'\mathbf{d}$, where $\mathbf{g}$ and $\mathbf{H}$ are the gradient and Hessian of E respectively, and $\mathbf{F}'$ is the adjoint operator. In this case, the gradient can be derived as

$$\mathbf{g}(\mathbf{x};\mathbf{x}_h) = -\mathbf{F}'\mathbf{d} = \int_w \int_{\mathbf{x}_m} ik\, A_s A_r D e^{-iw\tau}\, d\mathbf{x}_m\, dw \; . \tag{4}$$

where $k = w/\alpha$ is the spatial wavenumber. An approximate diagonal Hessian can be derived as

$$\mathbf{H} = \mathbf{F}'\mathbf{F} + \epsilon^2 \approx \int_w \int_{\mathbf{x}_m} k^2 A_s^2 A_r^2\, d\mathbf{x}_m\, dw + \epsilon^2(\mathbf{x};\mathbf{x}_h) \; , \tag{5}$$

resulting in the l_2 reflectivity solution

$$\grave{P}\acute{P}(\mathbf{x};\mathbf{x}_h) \approx -\frac{\mathbf{g}(\mathbf{x};\mathbf{x}_h)}{\mathbf{H}(\mathbf{x};\mathbf{x}_h)} \; . \tag{6}$$

The approximate diagonal Hessian solution (6) costs little more to implement than a standard prestack migration, but requires twice the memory in order to store the gradient and Hessian images separately. In particular, (6) involves two separate but simultaneous images to be evaluated, the gradient (numerator) being a weighted Kirchhoff prestack depth migration, and the approximate Hessian (denominator) being an accumulation of the squared migration weights.

Reflection angle estimation

An l_2 solution for the reflection angles Θ can be estimated directly from the reflection data D by substituting the solution (6) into the normal equation $\partial E/\partial\Theta = 0$. However, an efficient ad hoc solution is available based on physical intuition. Consider a fixed point $\mathbf{x}$ in the subsurface. As we migrate a constant offset section into $\mathbf{x}$, the angle θ_{sr} between the source and receiver rays ranges from $\theta_{sr} \approx 0$ at the midpoint position $\mathbf{x}_m = \mathbf{x}_{min}$, to $\theta_{sr} \approx 2\Theta$ near the specular midpoint, and back to $\theta_{sr} \approx 0$ at $\mathbf{x}_m = \mathbf{x}_{max}$. Analogously, the differential reflection coefficient R_{PP} varies from $R_{PP} \approx 0$ (diffraction) to $R_{PP} \approx \grave{P}\acute{P}(\Theta)$ (specular reflection), to $R_{PP} \approx 0$ (diffraction) again, over the same midpoint integration range. Hence, it is apparent that R_{PP} will attain a maximal peak amplitude at the specular midpoint, whereupon $R_{PP} = \grave{P}\acute{P}(\Theta)$ and $\theta_{sr} = 2\Theta$. This physical argument suggests performing a first moment weighted estimate of Θ as follows:

$$f(2\Theta(\mathbf{x};\mathbf{x}_h)) \approx \frac{\mathbf{g}_2(\mathbf{x};\mathbf{x}_h)}{\mathbf{H}_2(\mathbf{x};\mathbf{x}_h)} \tag{7}$$

where

$$\mathbf{g}_2(\mathbf{x};\mathbf{x}_h) = \int_w \int_{\mathbf{x}_m} |k\, A_s A_r D| f(\theta_{sr}) e^{-iw\tau}\, d\mathbf{x}_m\, dw \tag{8}$$

and

$$\mathbf{H}_2(\mathbf{x};\mathbf{x}_h) = \int_w \int_{\mathbf{x}_m} |k\, A_s A_r D| e^{-iw\tau}\, d\mathbf{x}_m\, dw + \lambda^2(\mathbf{x};\mathbf{x}_h)\ , \tag{9}$$

where λ^2 is another damping parameter, and $f(\Theta)$ is a function which can be arbitrarily chosen to optimize the estimate. In practice, choosing f to be a low power of the cosine function works well, such that $f \approx \cos^\nu \theta_{sr}$. I have found $\nu = 2$ works well by experience. It should be noted that the estimate (7) is very similar to the result of Bleistein (1987) for $\nu = 1$, except that the slightly different WKBJ weighting and the absolute value signs may add a certain robustness advantage, especially at subsurface points $\mathbf{x}$ where $|\grave{P}\acute{P}|$ is small or zero.

The two estimates $\grave{P}\acute{P}(\mathbf{x};\mathbf{x}_h)$ and $\Theta(\mathbf{x};\mathbf{x}_h)$ can be mapped uniquely to the desired output $\grave{P}\acute{P}(\mathbf{x};\Theta)$, which completes the least-squares angle-dependent reflectivity estimation.

Prestack time migration/inversion

In areas with weak lateral velocity variation, it has long been known that time migration followed by time-to-depth conversion is a good approximation for full prestack depth migration in a kinematic imaging sense, and is at least an order of magnitude more efficient. I claim the same is true for migration/inversion in a *dynamic* sense, where time migration approximations are used for the amplitude and ray dynamic variables as well as the standard kinematic approximations. Not everyone agrees (e.g., Berkhout, 1992, EAEG discussion period following the presentation by Lumley and Biondi, 1992).

In this study, I show the results of efficient time migration/inversion in a velocity model of weak lateral variation. I factor the WKBJ amplitudes A into components of source/receiver directivity and strength, geometric divergence, transmission loss, and intrinsic Q attenuation. In this example I implement WKBJ amplitude compensation for only source/receiver directivity and geometric divergence, assuming attenuation due to transmission and Q is negligible here. I represent the air-gun source with a $\cos^2\theta_s$ directivity to account for the free-surface and array effect. I represent the receiver directivity as $\cos^2\theta_r$ to account for the free-surface and hydrophone group effect. These directivity patterns are input parameters to be freely chosen by the user depending on source and receiver type, and whether marine or land acquisition.

I estimate the ray angles as follows. In a constant velocity earth, the straight raypath angle is given simply as:

$$\cos\theta_0 = \frac{\tau}{t} \ , \tag{10}$$

where τ is vertical migration pseudodepth, and t is migration hyperbolic traveltime. For the case of an rms time migration velocity field $v(x, y, \tau)$, I make the approximation that the take-off angle at the source or receiver surface is given by:

$$\cos\theta_{s,r} \approx [\cos\theta_0]^{+q} \ , \tag{11}$$

and the incident angle at the subsurface image point is:

$$\cos\theta_i \approx [\cos\theta_0]^{-q} \ , \tag{12}$$

where the exponent q is defined as:

$$q = \frac{v(x, y, \tau = 0)}{v(x, y, \tau)} \ . \tag{13}$$

For the divergence compensation, I use the standard geometric spreading approximation in an rms velocity field $v(x, y, \tau)$:

$$A_{div} \approx \frac{1}{v^2 t} \ . \tag{14}$$

These approximations are then used in the prestack migration/inversion to compute the gradient and Hessian terms of equations (4) and (5), resulting in final prestack time estimates of $\grave{P}\acute{P}(\mathbf{x}; \mathbf{x}_h)$ and $\Theta(\mathbf{x}; \mathbf{x}_h)$. These are then easily converted to depth by a simple vertical stretch algorithm in weakly lateral variable media, or by reverse-time extrapolation through an interval velocity model with strong time migration lateral positioning errors. Of course, in strong $v(x)$ media, time migration may not be appropriate at all even in a kinematic sense. However, many reservoir and exploration situations satisfy the time migration approximations well.

Impedance estimation

Once I have estimated $\grave{P}\acute{P}(\Theta(\mathbf{x}))$, an inverse problem for three isotropic elastic parameters can be posed. Under the assumption that *relative contrasts* in material properties are small at reflecting boundaries, and the reflection angles are well within the pre-critical region (Aki and Richards, 1980), a linearization of the Zoeppritz plane wave reflection coefficients can be made at every subsurface point $\mathbf{x}$:

$$\grave{P}\acute{P}(\Theta) \approx I_p c_1(\Theta) + I_s c_2(\Theta) + D c_3(\Theta) \ , \tag{15}$$

where $\{I_p, I_s, D\}$ are the relative contrasts in P impedance, S impedance and density at the reflecting boundary, and $\{c_1, c_2, c_3\}$ are known basis functions which are analytical in Θ. The three basis functions are plotted in Figure **??**, with c_1 at the top, c_2 at the bottom, and c_3 near the zero axis in the middle, and are given here analytically as:

$$\begin{aligned} c_1 &= 0.5 \sec^2 \Theta \\ c_2 &= -4\gamma^2 \sin^2 \Theta \\ c_3 &= 2\gamma^2 \sin^2 \Theta - 0.5 \tan^2 \Theta \end{aligned} \tag{16}$$

where γ is the shear to compressional velocity ratio v_s/v_p. I used a constant value of $\gamma^2 = 0.25$ in this data example, but it could be specified as a function $\gamma(\mathbf{x})$ if the appropriate v_p and v_s information is available. In fact, the basis functions c_i are not too sensitive to reasonable ranges of γ values.

In principle, any three elastic parameters $\{P, S, D\}$ can be chosen that span the $\grave{P}\acute{P}$ space. I choose the elastic *impedance* parameterization, because of its robust inversion properties for surface seismic geometries when a narrow (e.g., 5-35°) reflection illumination aperture is only available in the data. I explored this issue more completely in Lumley and Beydoun (1991), and it has recently become an active area of discussion in AVO inversion (e.g., De Nicolao et al., 1991).

In particular, I invert (15) at every subsurface location $\mathbf{x}$ by a least-squares method which bootstraps with offset and angle. The logic behind my approach is based on the properties of the basis functions $\{c_1, c_2, c_3\}$, as plotted in Figure **??**. I first find a least-squares estimate for I_p using only $\grave{P}\acute{P}$ values for which $\Theta \leq 15^\circ$. Next, I find a least-squares estimate for I_s using the $\grave{P}\acute{P}$ data in the range $10^\circ \leq \Theta \leq 40^\circ$ and using the estimate of I_p as a *constraint* on the system. Finally, if there are angles in the data greater than 35°, I perform a least-squares estimate for the density parameter using the I_p and I_s values as constraints. I have found this method to be a very robust procedure for estimating I_p and I_s (e.g., better than damped SVD), and also for demonstrating that little or no *independent* information on the contribution of density contrasts to a reflection in typical surface seismic geometries is invertible.

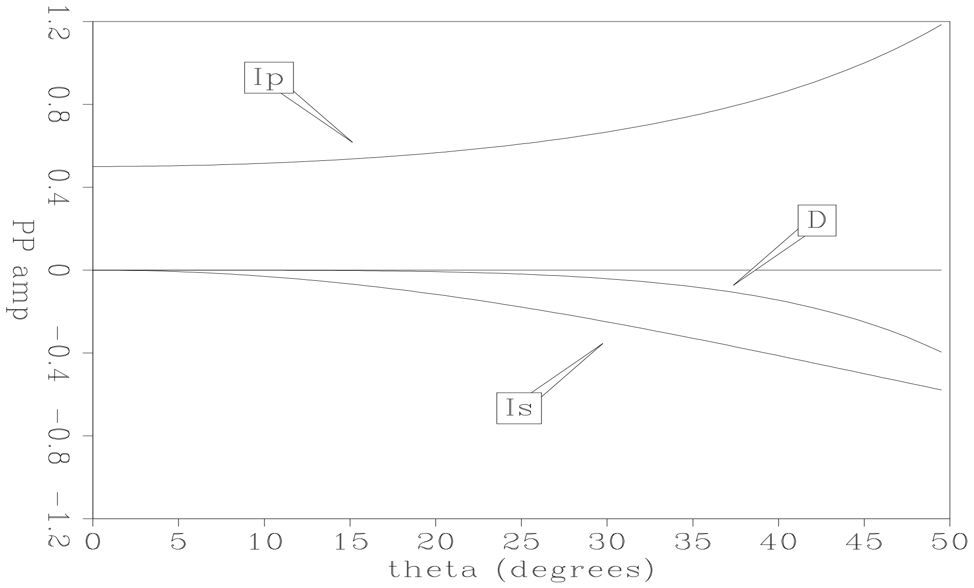

Figure 2: Impedance parameterization. Reflectivity unit impulse radiation curves (basis functions) $\{c_1, c_2, c_3\}$ for the impedance parameter set $\{I_p, I_s, D\}$. The uppermost curve is due to a unit perturbation in relative P impedance contrast alone, the lower curve is due to a unit perturbation in relative S impedance contrast alone, and the middle curve is due to a unit perturbation in relative density contrast alone. david3-imprad-ann [CR]

PILOT STUDY

I now briefly discuss the 2-D pilot study I have conducted to indicate the practical utility of my prestack impedance inversion theory and algorithms.

Figure **??** shows two CMP gathers from a 1970's vintage 2-D marine survey. The gathers are from midpoint location 1 km and 2 km respectively, along the stacked section shown in Figure **??**. The CMP gathers exhibit a strong amplitude-offset (AVO) reflectivity response on the reflected event at about 2.3 seconds zero-offset time. Note the offset-variability in the raw AVO response. An advantage of prestack migration/inversion is that it uses an estimated variable velocity field to compensate for such wave-based focusing/defocusing effects on amplitudes in raw data.

The stacked section shows a few strong reflectors in the 2.3-2.5 second range, which are known to correspond to the reservoir interval of a producing gas field (Kjartansson, 1979). The offset stack across any AVO character will tend to invalidate the common assumption that the stacked section is an approximation of P impedance contrasts. This would have a negative impact on "poststack impedance inversion" for example.

Figure **??** shows the migration velocity semblance panels corresponding to the two CMP positions. The overlain black curves are the "optimal" migration velocities picked by a nonlinear Monte Carlo automatic search algorithm (Lumley, 1992b). After all 100 semblance scans are searched for the optimal migration velocity trajectory, the results are slightly smoothed and contoured in Figure **??**. The contours of the migration velocity field range from 1.6 km/s at the top to 2.3 km/s at the bottom, in 0.1 km/s intervals. The low velocity zone at the far left is apparently real, when the semblance scans at this location are examined. Also, note the low rms velocity zone at 2.3 seconds in the right scan, which will later be shown to correlate with an impedance anomaly indicative of increased gas saturation. This velocity model is used for the subsequent reflectivity estimation and impedance inversion.

Given 4800 input seismic traces, I perform 48 constant offset migrations ranging from offsets of 0.25 km to 2.65 km in 50 m increments. Figure **??** shows two Common Reflection Point (CRP) slices of the constant offset migration cube, each slice taken at a fixed midpoint position of 1 km and 2 km respectively, to correspond with the surface positions of the previous figures. This figure corresponds to the prestack-migrated equivalent of an NMO/DMO amplitude-corrected CMP gather in conventional AVO processing. The midpoint coordinate direction is perpendicular to the plane of the page. The top of the reservoir is at 2.3 seconds, and we are looking at how the migrated reflectivity estimate varies as a function of offset: $\grave{P}\acute{P}(\mathbf{x};\mathbf{x}_h)$. At surface position 1 km, the top panel shows what appears to be a weak negative polarity reflection at the top of the reservoir, and the reflection strength approximately constant, although somewhat irregular, with increasing offset (angle). At the 2 km surface position (lower panel), the top of the reservoir appears to have changed to a somewhat stronger negative polarity and an increase in negative amplitude with increasing offset (angle). This difference suggests that the material properties in the reservoir have changed spatially from surface position 1 km to 2 km.

Figure **??** is the same plot as Figure **??**, except the quantity being plotted is the incident reflection angle $\Theta(\mathbf{x};\mathbf{x}_h)$ instead of the reflectivity itself. The contours range from reflection angles of 5° at near offsets to 30° at the farthest offsets, in increments of 5°. Given the functions $\grave{P}\acute{P}(\mathbf{x};\mathbf{x}_h)$ and $\Theta(\mathbf{x};\mathbf{x}_h)$ estimated from the data, the two can be combined to give the estimate of reflectivity as a function of reflection angle: $\grave{P}\acute{P}(\Theta(\mathbf{x}))$.

For comparative purposes, I plot the prestack migrated stack in Figure **??**. This is obtained efficiently by merely summing the $\grave{P}\acute{P}(\mathbf{x};\mathbf{x}_h)$ gathers over the offset coordinate $\mathbf{x}_h$. It will be interesting to compare this image with the P and S impedance contrast maps.

Next, at each point in earth, I perform the linearized inversion of $\grave{P}\acute{P}(\Theta(\mathbf{x}))$ to estimate the elastic parameters $\{I_p, I_s, D\}$. The P impedance contrast section is shown in Figure **??**, the S impedance contrast section is shown in Figure **??**, and the density contrast section is shown in Figure **??**. As expected, the S/N ratio and stability of the inversion is good for P impedance, medium for S impedance, and very poor for density. Figure **??** justifies my claim that there is little or no useful *independent information* about subsurface density contrasts in standard acquisition geometry surface seismic data. Disregarding density, there appear to be some significant differences in information content comparing the P and S impedance contrast sections, especially near the 2 km midpoint location. Also, the migration stack of Figure **??** is most similar to the P impedance contrast section of Figure **??**, as expected, but does have some orthogonal information content along the reservoir reflector at 2.3 seconds in the distance range of 1.2–1.6 km, for example.

A simple multiplication of the P and S sections produces an interesting $P * S$ anomaly map, as shown in Figure **??**. In "normal" rock sequences, the P and S impedance contrasts are usually of the same polarity, and hence plot dark gray to black (blue) in Figure **??**. However, in a transition zone of changing rock properties, say from brine to gas-filled porespace, the P and S impedance contrasts may be of opposite polarity, and will plot as white (red) regions in Figure **??**. It is interesting to note that the white (red) anomalous regions of Figure **??** are well localized to the reflectors associated with the producing gas reservoir interval, and also importantly, *nowhere else* in the section.

This result indicates that the prestack impedance inversion theory and algorithms have been qualitatively tested and give reasonable physical results, since an AVO amplitude anomaly and a $P*S$ impedance anomaly has been unambiguously detected by the method at the zone of a known gas producing reservoir interval.

CONCLUSIONS

This pilot study indicates that prestack impedance inversion produces P and S impedance information which correlates with the presence of a known gas producing reservoir, at least in a qualitative sense. There is clear potential for mapping spatial changes in reservoir rock properties and pore-fluid constituents from 3-D surface seismic data, which may in turn help production geophysicists and engineers better characterize and understand a given reservoir. Obviously a more quantitative test would need to include detailed well control, reservoir geology and reservoir production data, as is part of my ongoing research.

ACKNOWLEDGMENT

I thank Wafik Beydoun (Elf Research UK) for many stimulating brainstorming sessions we have had together on the topic of migration/inversion. Thanks also to Wafik for arranging my trip to Elf to install the latest version of my inversion codes, where

I hope they will be thoroughly tested on many real data examples for inversion robustness and utility.

REPRODUCIBILITY

Because of the sensitive thesis-related nature of these algorithms, I am not releasing this working code on the CD version of this report. Therefore, you will not be able to rebuild my examples starting from the raw input data. General release of inversion code will coincide with the thesis publication. Special arrangements to install the code at SEP sponsor sites can be discussed on an individual basis.

REFERENCES

Aki, K., and Richards, P. G., 1980, Quantitative seismology: W. H. Freeman and Company.

Beylkin, G., 1985, Imaging of discontinuities in the inverse scattering problem by inversion of a causal generalized Radon transform: J. Math. Phys., **26**, 99–108.

Beydoun, W. B., and Mendes, M., 1989, Elastic ray-Born l-2 migration/inversion: Geophys. J., **97**, 151–160.

Bleistein, N., 1987, On the imaging of reflectors in the earth: Geophysics, **52**, 931–942.

Crase, E., Pica, A., Noble, M., McDonald, J., and Tarantola, A., 1990, Robust elastic nonlinear waveform inversion: application to real data: Geophysics, **55**, 527–538.

Cunha Filho, C., 1992, Elastic modeling and migration in earth models: Ph.D. thesis, Stanford University.

de Bruin, C., 1992, Linear AVO inversion by prestack depth migration: Ph.D. thesis, Delft University, The Netherlands.

De Nicolao, A., Drufuca, G., and Rocca, F., 1991, Eigenvectors of linearized elastic inversion: 61st Ann. Internat. Mtg., Soc. Expl. Geophys., Expanded Abstracts, 1017–1020.

Kjartansson, E., 1979, Attenuation of seismic waves in rocks and applications in energy exploration: Ph.D. thesis, Stanford University.

Lumley, D. E., and Beydoun, W. B., 1991, Elastic parameter estimation by Kirchhoff prestack depth migration/inversion: Stanford Expl. Proj. Report, **70**, 165–192.

Lumley, D. E., 1992a, Estimation of elastic specular reflectivity by Kirchhoff prestack depth migration: WKBJ least-squares theory: Stanford Expl. Proj. Report, **75**, 355–368.

Lumley, D. E., 1992b, Monte Carlo automatic velocity picks: Stanford Expl. Proj. Report, **75**, 1–20.

Lumley, D. E., and Biondi, B., 1992, Kirchhoff 3-D prestack time migration on a massively parallel supercomputer: 54th Ann. Meeting of the Eur. Assoc. of Expl. Geophys., Expanded Abstracts, 286–287.

Lumley, D. E., 1993, Angle-dependent reflectivity estimation: Stanford Expl. Proj. Report, **77**, this report.

Nur, A., 1989, Four dimensional seismology and (true) direct detection of hydrocarbons: The petrophysical basis: The Leading Edge, **9**, 30–36.

Parsons, R., 1986, Estimating reservoir mechanical properties using constant offset images of reflection coefficients and incident angles: 56th Annual Internat. Mtg., Soc. Expl. Geophys., Expanded Abstracts.

Tarantola, A., 1986, A strategy for nonlinear elastic inversion of seismic reflection data: Geophysics, **51**, 1893–1903.

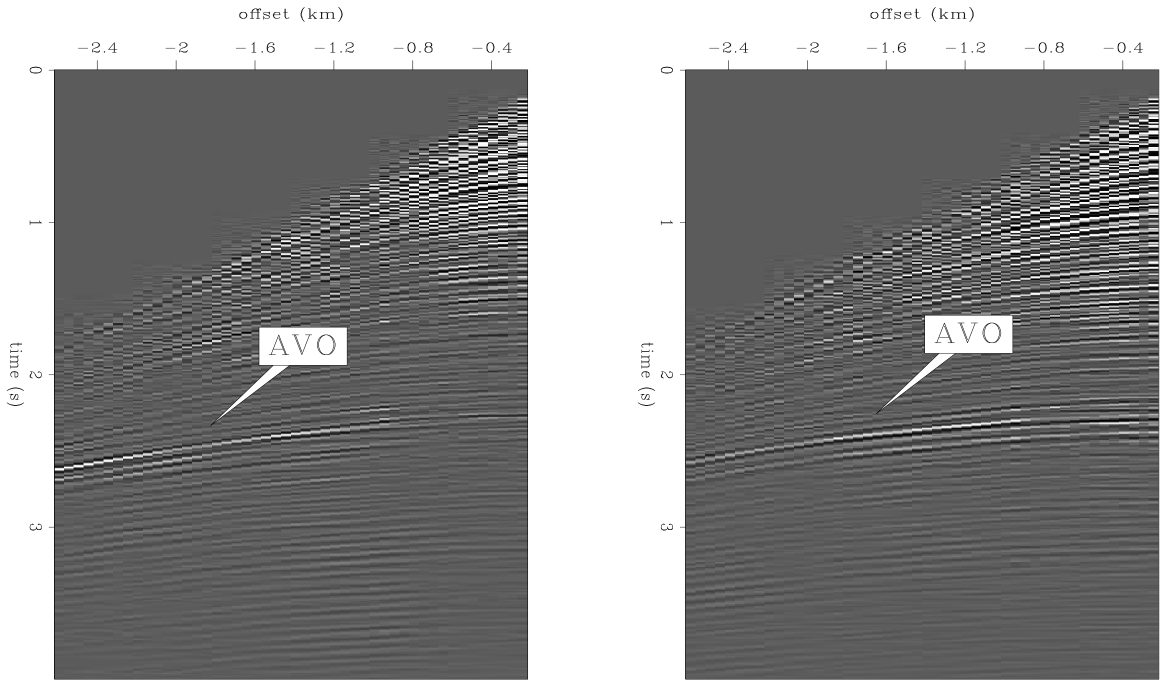

Figure 3: CMP gathers at surface positions 1 km and 2 km. Note the bright AVO response at 2.3 seconds due to the gas reservoir at depth. david3-cmps-ann [CR]

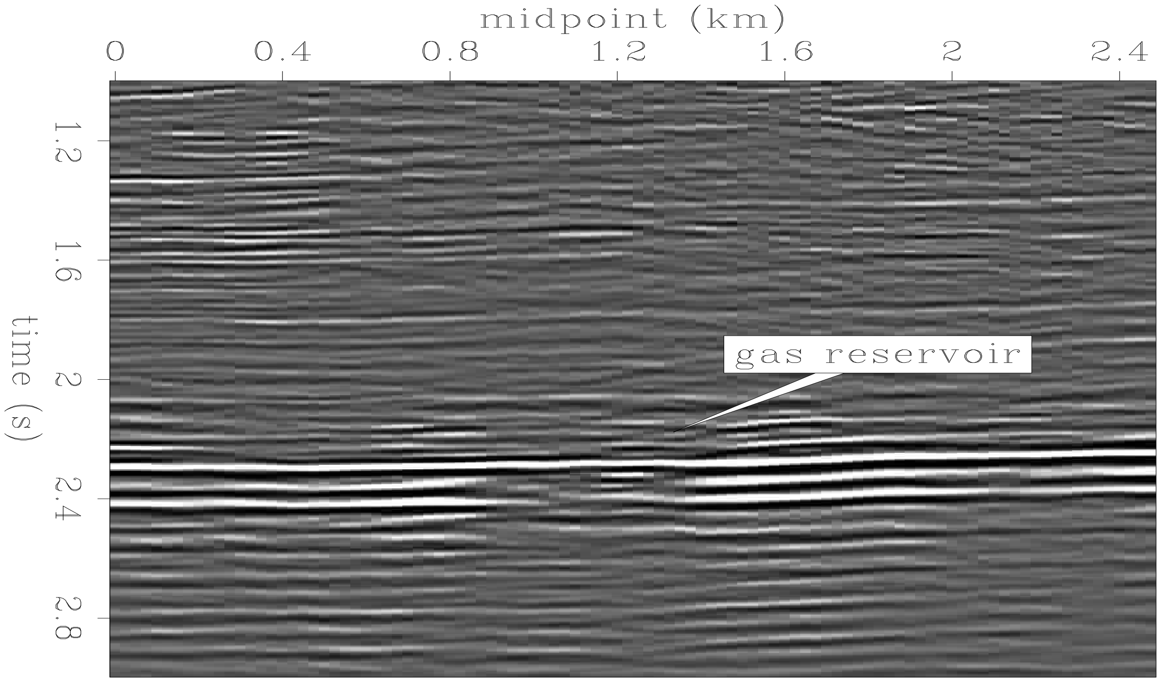

Figure 4: Stacked section structural image. The bright reflectors at 2.3 seconds are associated with a gas production reservoir interval. david3-stack-ann [CR]

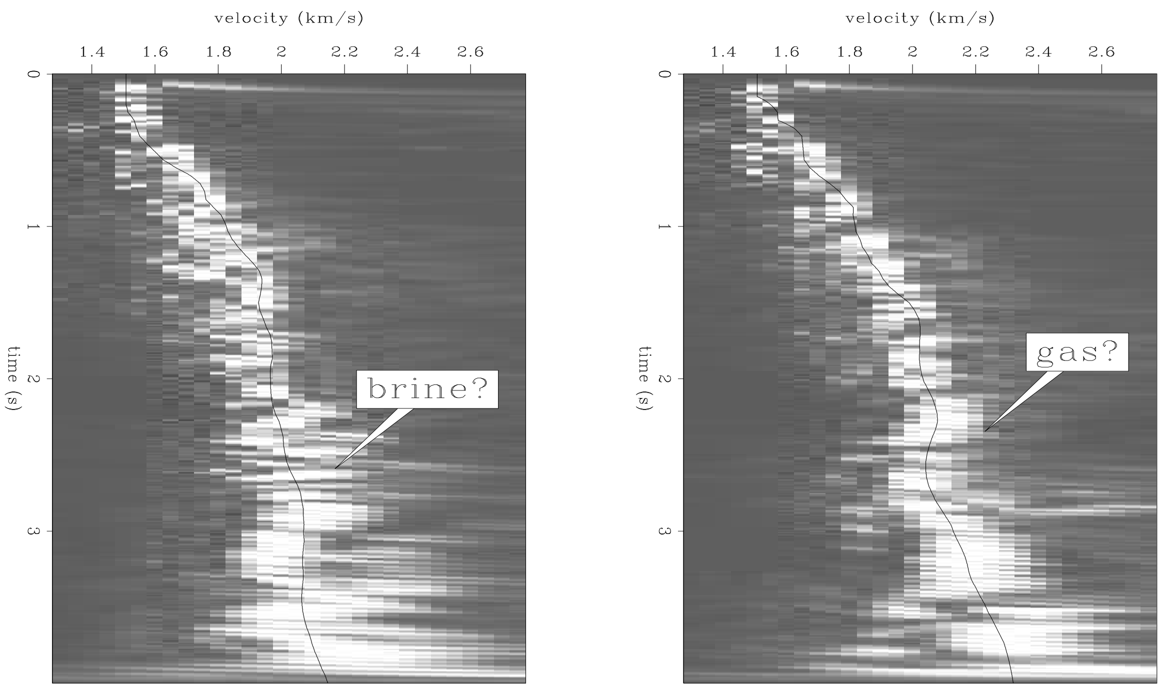

Figure 5: Migration velocity semblance scans at surface midpoint positions 1 km and 2 km. The overlain curves are the automatic Monte Carlo velocity picks. david3-vscans-ann [CR]

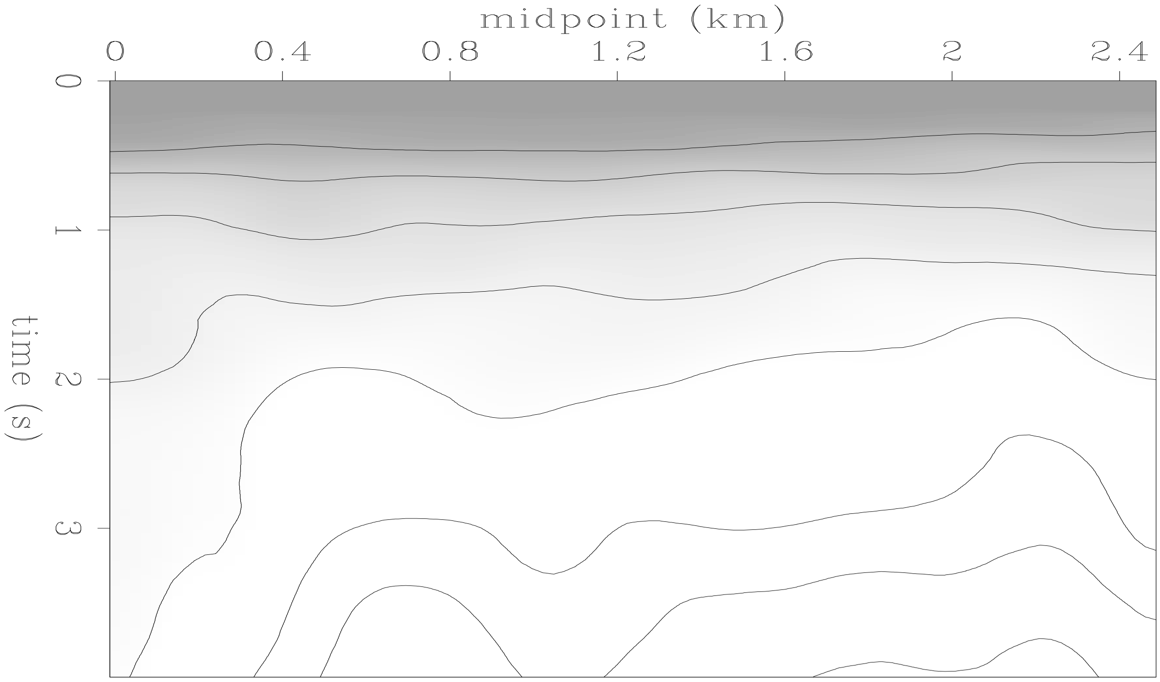

Figure 6: Migration velocity field, obtained by picking 100 migration semblance scans and slight smoothing. david3-migvel [CR]

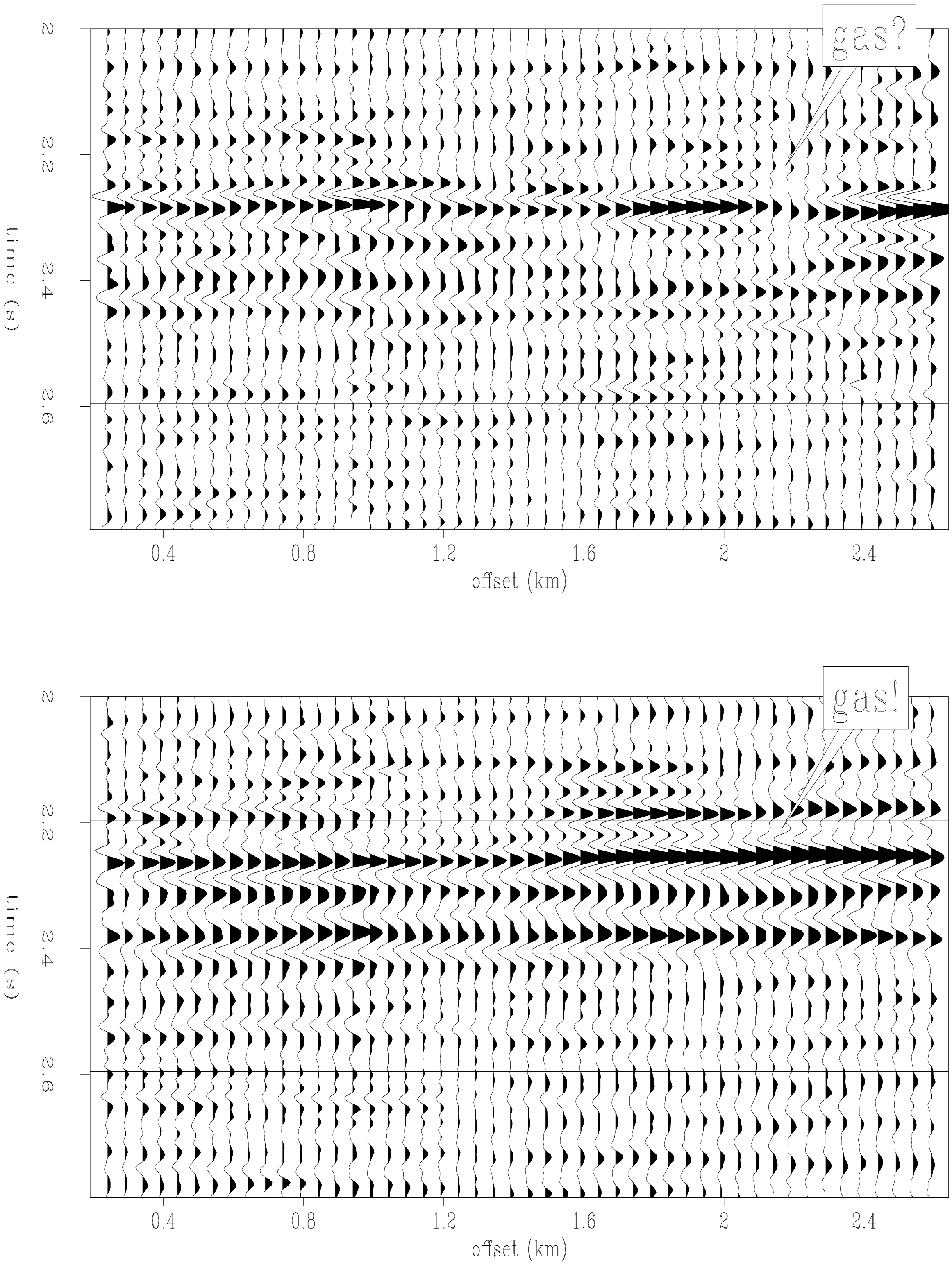

Figure 7: Migrated CRP (Common Reflection Point) reflectivity gathers. The top panel is at surface location 1 km, the lower panel at 2 km. The midpoint coordinate direction is perpendicular to the plane of the page. david3-crps-ann [CR]

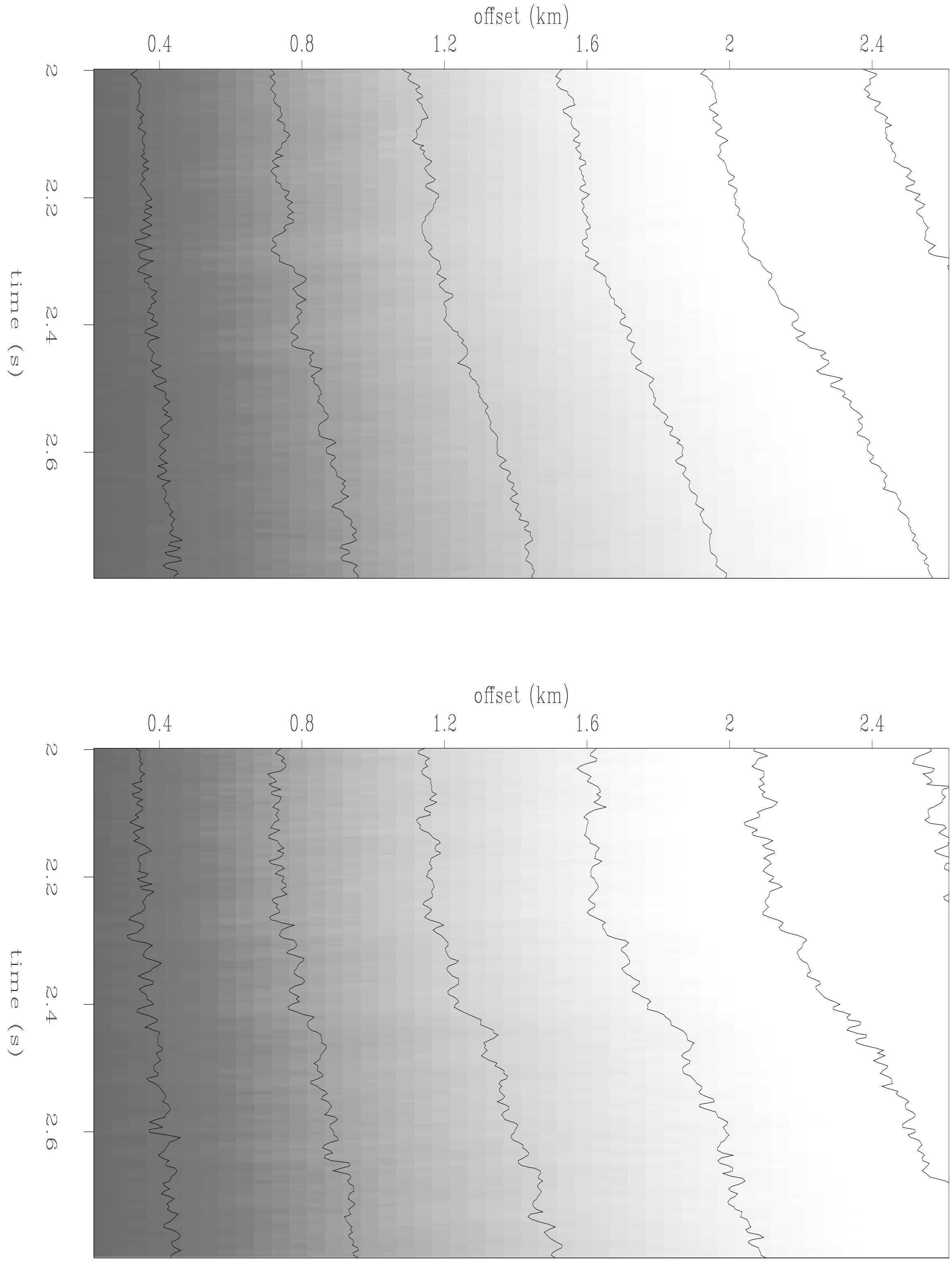

Figure 8: Migrated CRP reflection angle gathers. Reflection angle contours range from 5° at near offsets to 30° at far offsets, in 5° intervals. david3-thetas [CR]

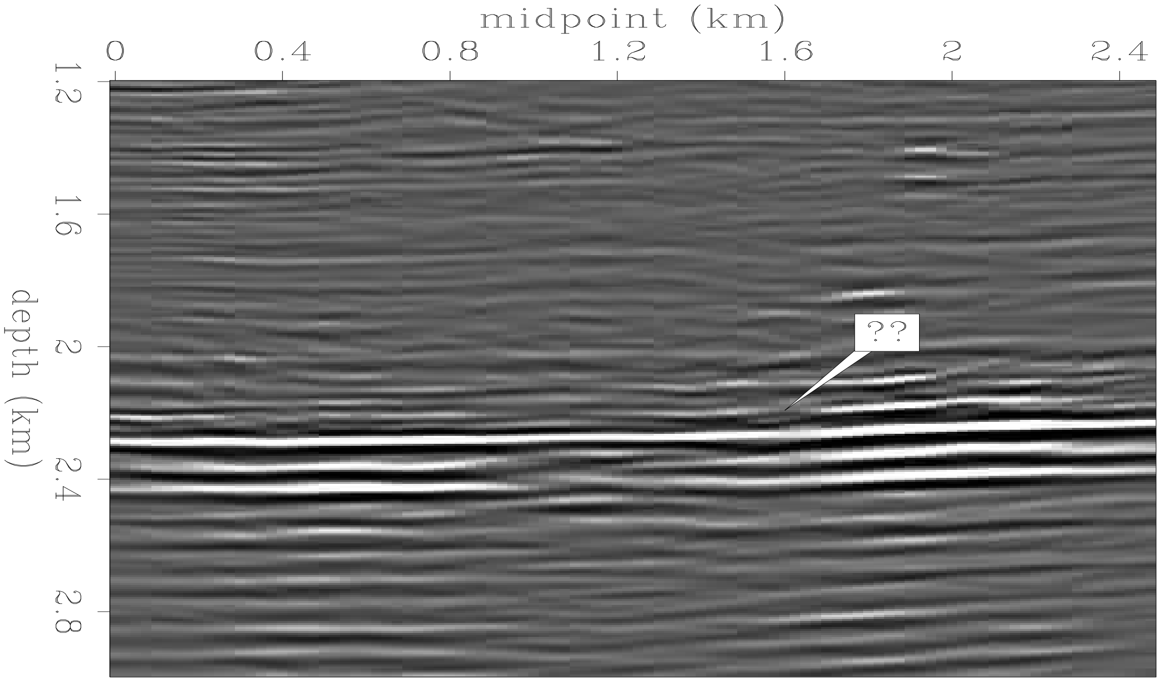

Figure 9: Migrated structural image obtained by stacking the migrated CRPs over offset. david3-mig-ann [CR]

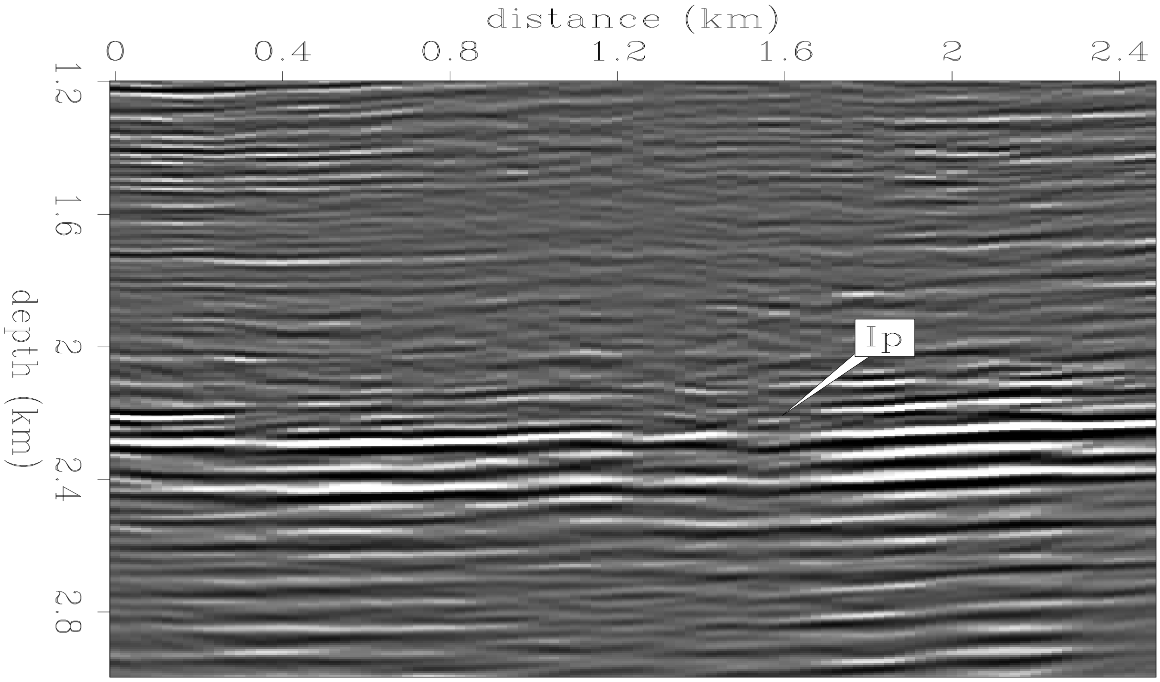

Figure 10: P impedance contrast section. david3-Pimp-ann [CR]

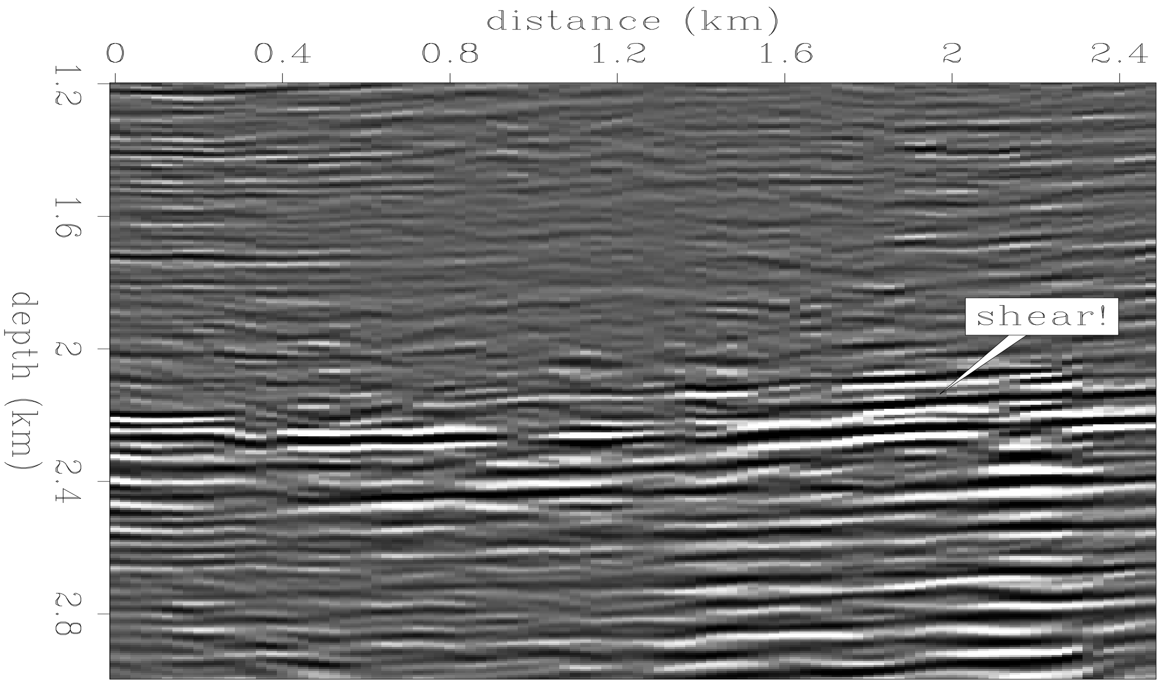

Figure 11: S impedance contrast section. david3-Simp-ann [CR]

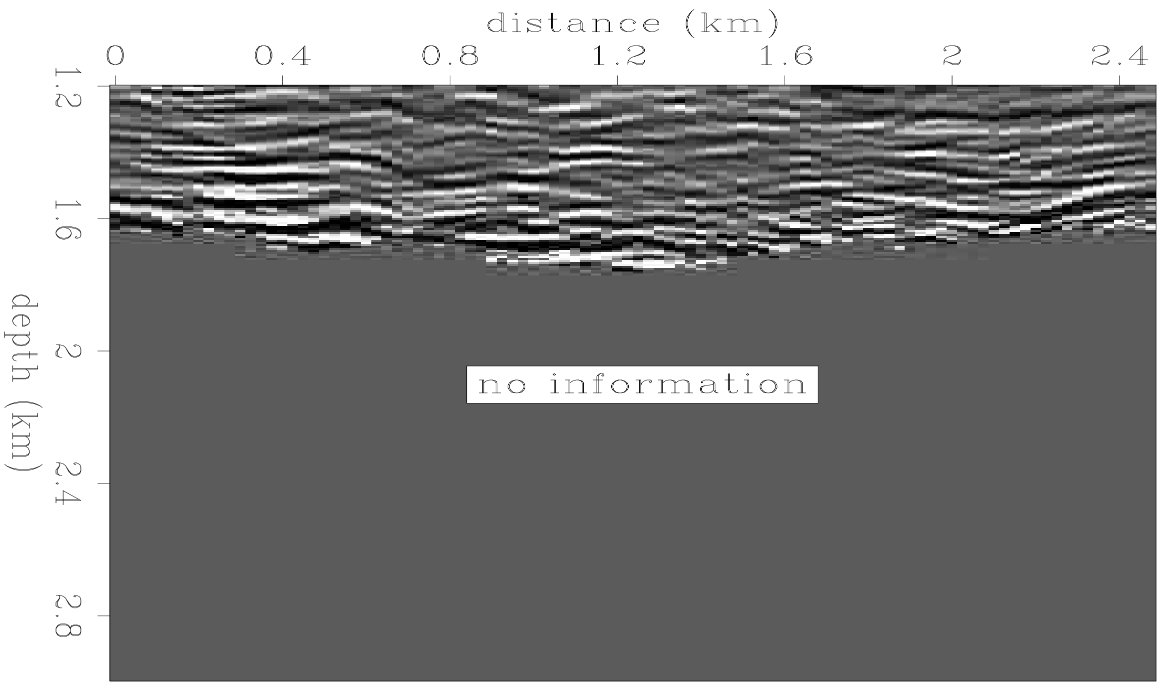

Figure 12: Density contrast section. david3-Dens-ann [CR]

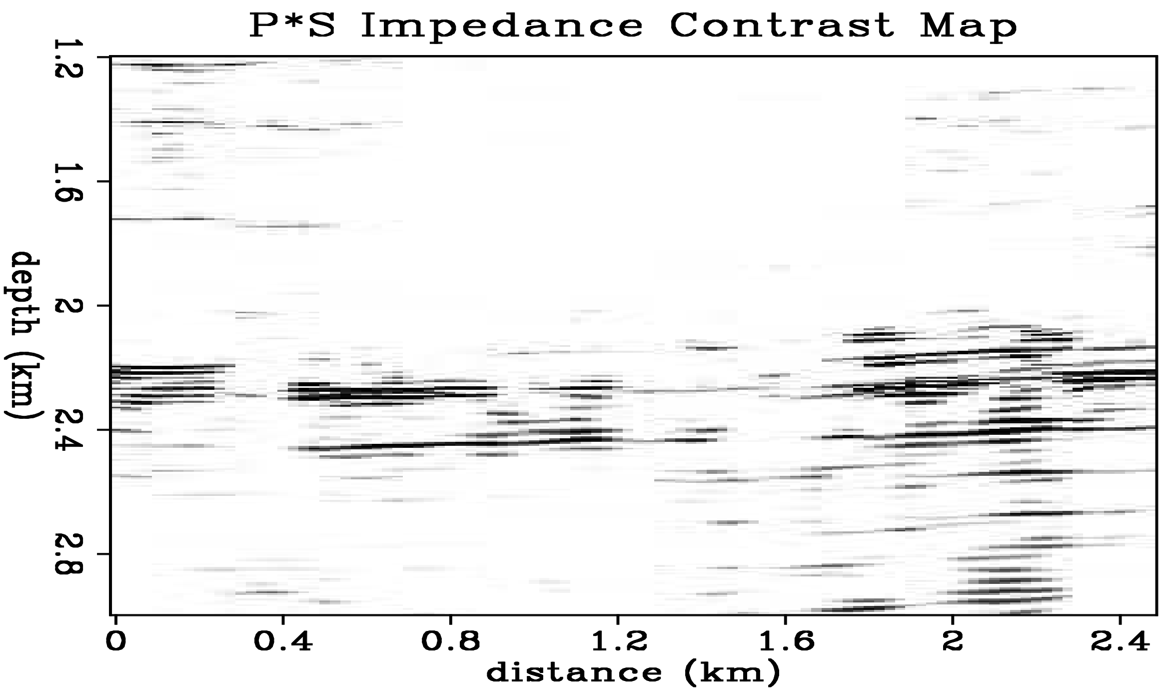

Figure 13: $P * S$ impedance anomaly section. Note the bright anomaly, probably due to increased gas saturation, near the surface midpoint position at 2 km. david3-PSmapC [CR]